



APPENDICES

ลิขสิทธิ์มหาวิทยาลัยเชียงใหม่

Copyright[©] by Chiang Mai University

All rights reserved

APPENDIX A

Row-wise standardization technique

The assumption of this technique is that the variation of the responses of sensors, due to the gas concentration, should exhibit a linear relationship to each other for a gas. To perform the row-wise standardization, the responses need to be subtracted with base-line to obtain positive data. The response is transformed into a matrix which the number of column and row equal to the number of sensors and samples, respectively. The mean and standard deviation of each rows is computed. Then each element in the matrix will be subtracted with the mean and divided by the standard deviation of that row. The following shows mathematical step to prove that a unique pattern will be obtained for a gas.

Let \bar{x}_j be a set of response of sensor j on several concentration of a gas,

$$\bar{x}_j = \begin{bmatrix} x_{1j} \\ x_{2j} \\ \vdots \\ x_{mj} \end{bmatrix} \quad (A.1)$$

where m is number of sample and suppose that any \bar{x}_j can be written in the term of \bar{x}_l approximately in linear relationship for that gas.

$$\bar{x}_j = a_j \bar{x}_l + b_j \quad (A.2)$$

Subtract \bar{x}_j with b_j ,

$$\bar{y}_j = \bar{x}_j - b_j = a_j \bar{x}_I \quad (\text{A.3})$$

Let Y be a matrix composing of $\{\bar{y}_j\}$

$$Y = \begin{bmatrix} y_{11} & y_{12} & \cdots & y_{1n} \\ y_{21} & y_{22} & \cdots & y_{2n} \\ \vdots & \vdots & \ddots & \vdots \\ y_{m1} & y_{m2} & \cdots & y_{mn} \end{bmatrix} \quad (\text{A.4})$$

where n is number of sensor. The mean and standard deviation of row i can be expressed as

M_i = mean of row i of Y

$$M_i = \frac{1}{n} \sum_j^n y_{ij} = \frac{1}{n} \sum_j^n a_j y_{i1} \quad (\text{A.5})$$

S_i = standard deviation of row i of Y

$$S_i = \sqrt{\frac{1}{n-1} \left(\sum_j^n a_j^2 - \frac{1}{n} \left(\sum_j^n a_j \right)^2 \right)} \quad (\text{A.6})$$

To perform row-wise standardization to the data, Y , the element y_{ij} will be subtracted with M_i and then divide by S_i . Finally, unique values of data for each gas are derived after performing standardization.

$$y'_{ij} = \frac{y_{ij} - M_i}{S_i}$$

$$\begin{aligned}
 \vec{y}_{ij} &= \frac{y_{ij} - \frac{1}{n} \sum_j^n a_j y_{i1}}{\sqrt{\frac{1}{n-1} \left(\sum_j^n a_j^2 - \frac{1}{n} \left(\sum_j^n a_j \right)^2 \right)}} \\
 \vec{y}_{ij} &= \frac{a_j - \frac{1}{n} \sum_j^n a_j}{\sqrt{\frac{1}{n-1} \left(\sum_j^n a_j^2 - \frac{1}{n} \left(\sum_j^n a_j \right)^2 \right)}} = const. \tag{A.7}
 \end{aligned}$$

This indicates that value of each element in the matrix depends only on sensor.

APPENDIX B

Principal component analysis

PCA is unsupervised pattern recognition method. It means that PCA do not need to know the class of samplings before analysis. When PCA is applied to a data matrix, it split the data matrix to two matrixes, called scores and loadings as shown in Fig. B.1. The scores plot shows how separate the samplings are, in general. For the data having less than four variables, it is not necessary to apply PCA. The plot of the original data can show the separation of samplings. However for a huge number of variables, PCA is needed because it is also a method to reduce the dimension of data matrix. By the meaning of the name “principal component”, most information is in the principal components after performing PCA.

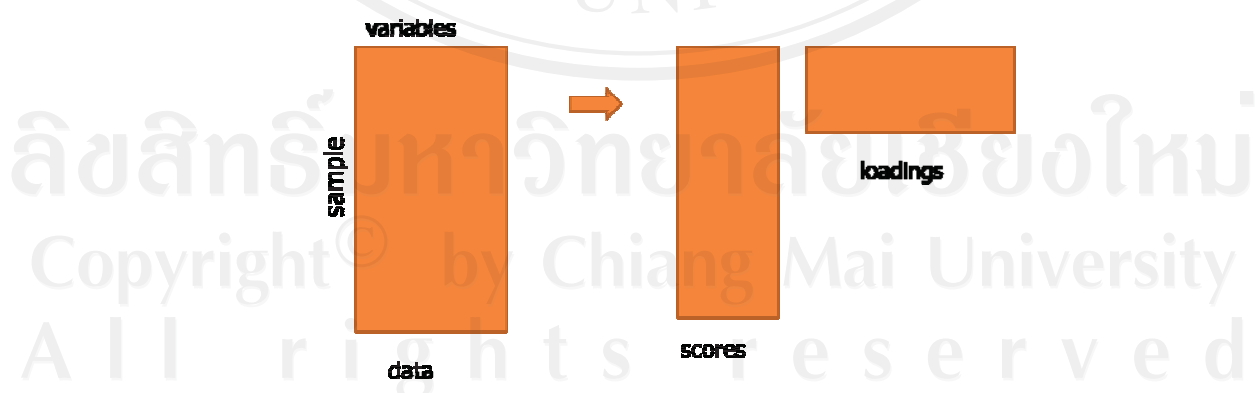


Figure B.1 Illustration of the output of applying PCA to data matrix.

Here, an example is shown for how to perform PCA mathematically. Suppose that PCA is applied to data matrix of 10X2 as shown in Fig. B.2, mean of each variable is calculated firstly. Elements in a variable are then subtracted by its mean. This process is called “centering” because each element in a new matrix got lay around zero. Next step is to calculate the covariance matrix by using following equation

$$Cov(X, Y) = \frac{\sum_{i=1}^n (x_i - \bar{x})(y_i - \bar{y})}{n-1} \quad (B.1)$$

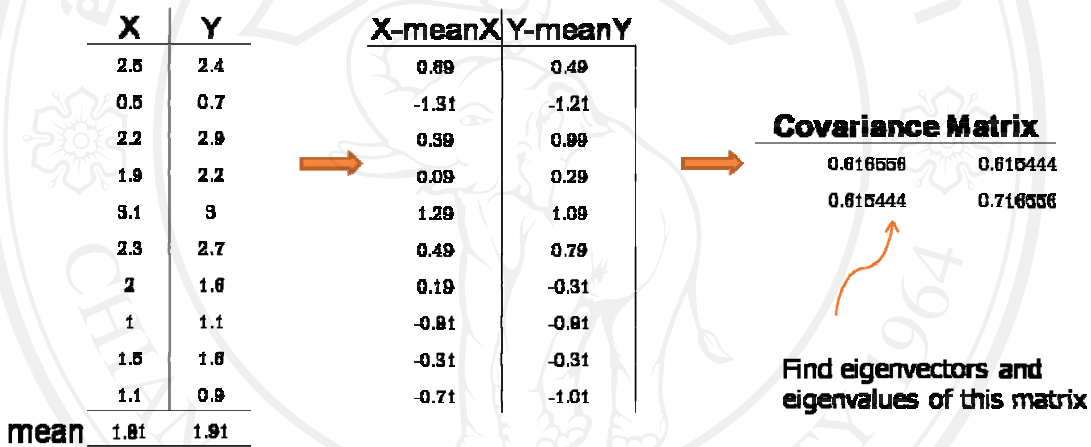


Figure B.2 Calculation of PCA

Eigenvalues and eigenvectors of covariance matrix are then calculated. The eigenvectors represent the new components whereas the eigenvalues indicate the scores of information and the component having highest score is the principal component. The scores in Fig. B.1 is the product of the centering matrix and eigenvectors. Finally the visualization of the separation of the samplings is obtained from the scores plot as shown in Fig. B.3.

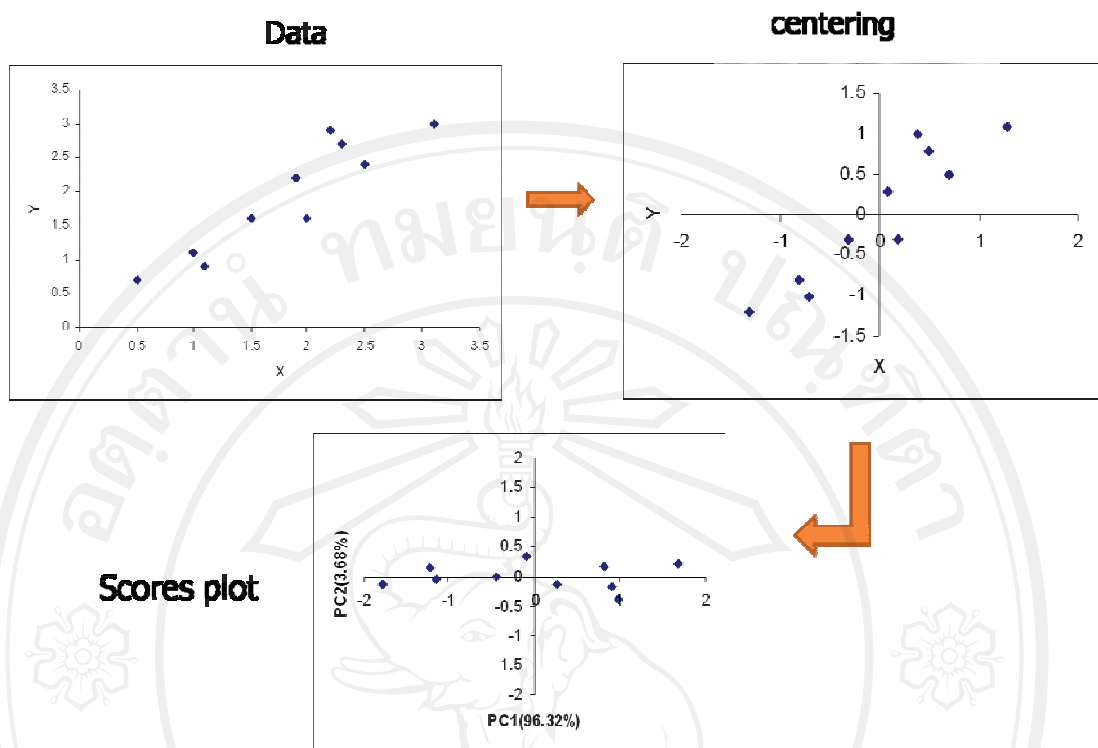


Figure B.3 The evolution of plot of data in PCA.

ลิขสิทธิ์มหาวิทยาลัยเชียงใหม่
 Copyright[©] by Chiang Mai University
 All rights reserved

APPENDIX C

Linear discriminant analysis

LDA is a supervised pattern recognition method which can be used to make a model for prediction. It needs to know the class of the samplings in learning step. The calculation in LDA, shown in Fig. C.1, is similar to that in PCA but more complex. The calculation in LDA divides into two parts, called classification and visualization. In both calculations the covariance of each class is needed. The within class covariance, C_w , can be calculated by using the equation C.1 and new feature matrix is calculated by using the equation C.2.

$$C_w = \frac{1}{20} \sum_i^4 C_i \quad (C.1)$$

$$\text{new feature matrix} = C_w^{-1} x (C_t - C_w) \quad (C.2)$$

where C_i is the covariance of class i which can calculate by using the equation B.1. The visualization of the separation of sampling can be obtained by finding eigenvectors and eigenvalues of the new feature matrix. The new data matrix can be got from the product of eigenvectors and original data matrix. The plot of the first and second component is the visualization of the separation.

The calculation in classification, discriminant functions, which are the linear combination of the original variables, are calculated for the sampling k by using following equation

$$f_i = u_i C_w^{-1} x_k^T - 0.5 u_i C_w^{-1} u_i^T - \ln(p_i) \quad (C.3)$$

$i = 1, 2, 3, \dots, \text{number of class}$

where f_i = discriminant function of the sampling k for class i

u_i = row matrix of mean of class i

C_w = within class covariance

x_k = the sampling k

p_i = prior probability of class i

The number of discriminant functions of the sampling k is equal to the number of classes. The sampling k is assigned to the class that the discriminant function is maximum.

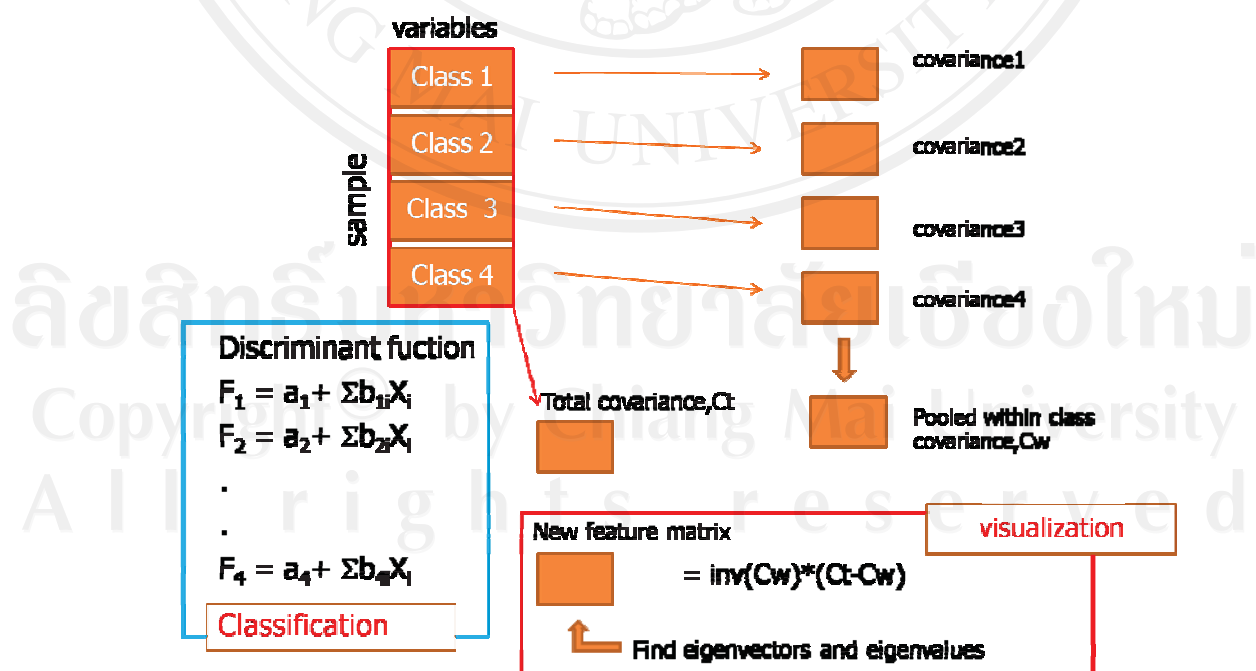


Figure C.1 Calculation of LDA

Stepwise linear discriminant analysis (step-LDA)

Step-LDA is feature selection method that finds an optimal set of variables (sensors) for a special classification. Purpose of the step-LDA is to remove unnecessary variables (or sensors) from the data matrix by using Wilks' lambda as a criterion of selection. Wilks' lambda can be calculated by following equation

$$\text{Wilks' lambda} = \frac{\det|C_w|}{\det|C_t|} \quad (\text{C.3})$$

Smaller value of Wilks' lambda means better separation between classes. Fig. C.2 shows how the step-LDA works. If the taken variable improves the Wilks' lambda significantly, it will be added in the model. Vice versa, the variable in model will be removed if it degrades the Wilks' lambda.

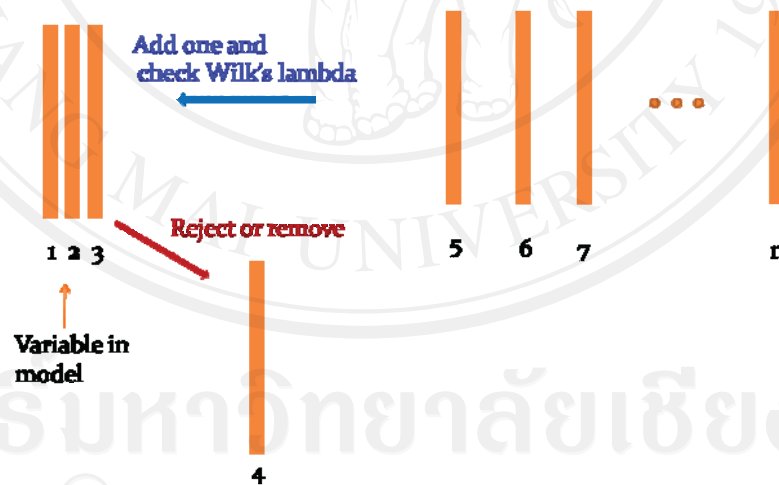


Figure C.2 Selection of variables by step-LDA method

APPENDIX D

PAPER PUBLICATIONS

Paper publications

Paper I S. Phadungdhitidhada, P. Mangkorntong, S. Choopun, and N. Mangkorntong, “Raman scattering and electrical conductivity of nitrogen implanted MoO₃ whisker”, *Ceram. Int.*, 2008, 34:1121.

Paper II S. Phadungdhitidhada, P. Mangkorntong, S. Choopun, N. Mangkorntong, and D. Wongratanaaphisan, “Synthesis of MoO₃ nanobelts by medium energy nitrogen ion implantation”, *Mater. Lett.* 65 (2011) 568-571.

Submitted article

Paper III S. Phadungdhitidhada, S. Thanasanvorakun, P. Mangkorntong, S. Choopun, N. Mangkorntong, D. Wongratanaaphisan, “SnO₂ nanowires mixed nanodendrites for high ethanol sensor response”, submitted for publication in *Curr. Appl. Phys.*

Paper I



Available online at www.sciencedirect.com

ScienceDirect

Ceramics International 34 (2008) 1121–1125

CERAMICS
INTERNATIONAL

www.elsevier.com/locate/ceramint

Raman scattering and electrical conductivity of nitrogen implanted MoO_3 whiskers

S. Phadungdhitdhada ^{*}, P. Mangkorntong, S. Choopun, N. Mangkorntong

Department of Physics, Faculty of Science, Chiang Mai University, Chiang Mai 50200, Thailand

Available online 5 October 2007

Abstract

Whiskers of MoO_3 have been grown by a thermal transport process. A set of samples was then implanted with nitrogen ions at a dose of 5×10^{16} ion/cm². The implanted whiskers changed from transparent to semi-transparent. Raman spectroscopy of the whiskers was observed and compared with those of unimplanted whiskers. The results revealed that the Raman intensity of the implanted whiskers was decreased about 10 times with respect to that of unimplanted whiskers. Only the case of the wave propagation parallel to the a -axis, a lower suppression ratio of the B_{3g} modes was observed. No extra mode due to the nitrogen implantation was observed. This indicates that implantation could only induce defects and oxygen vacancies but not the structural transformation. From electrical conductivity and Hall measurement, it was found that the whiskers exhibited an n-type semiconductor and its conductivity drastically increased due to the defects and oxygen vacancies.

© 2007 Elsevier Ltd and Techna Group S.r.l. All rights reserved.

Keywords: Ion implantation; Raman spectroscopy; Thermal transport; MoO_3 whisker

1. Introduction

Molybdenum trioxide (MoO_3) is a layered material which can be used in various types of applications. These include catalysts, photoluminescence, photochromisms, electrochromisms, sensors, and batteries [1]. Due to its optical and electronic properties, MoO_3 has become a promising material for applications in electrochromic systems ranging from microbatteries and gas sensing to devices for information displays [2].

Ion implantation is known as an effective technique to change some physical properties of a material such as electrical property [3]. MoO_3 is a wide band and indirect gap, which is an insulator at room temperature. The implantation of hydrogen ion into MoO_3 pellet to form MoO_3 bronze has been conducted previously [4]. The details of Raman spectra of MoO_3 single crystal and powder have also been realized and reported [5]. The influence of different amounts of oxygen vacancies on the Raman spectra of MoO_{3-x} samples with MoO_3 structure have been studied by Dieterle et al. [6]. They found that I_{283}/I_{290} has a linear relationship with O:Mo ratio. However, the intensity of

each Raman peak of the anisotropic crystal structure of MoO_3 is strongly dependent on the orientation of crystal and polarization of the laser source. So far, only the parallel and perpendicular to the c -axis have been reported [7].

In this research, the nitrogen implantation of MoO_3 has been performed for the first time and their properties have been studied. The Raman spectroscopy of all possible polarization and orientation of the MoO_3 whiskers have also been carried out and described in this paper.

2. Experimental procedure

In this research, the MoO_3 whiskers were grown by using the vapor transport method. Details regarding to crystal growth technique and identification of the whiskers can be found in [8]. The MoO_3 whisker specimen was prepared by attaching a set of whiskers on to an aluminium plate using silver paste. The dimensions of whiskers were approximately 10 mm in length, 1–2 mm in width and 3–5 μm in thickness, respectively. Nitrogen was induced into the specimen by using the ion implantation technique. The 150-kV ion implantor at Department of Physics, Chiang Mai University [9] was used to perform this process. The nitrogen ions were extracted from the ion source and moved forward directly to the target without using the mass analyzer, so that both N^+ and N_2^+ were in the

^{*} Corresponding author. Tel.: +66 53 943 375; fax: +66 53 357 511.

E-mail address: surelity@gmail.com (S. Phadungdhitdhada).

beam. The nitrogen ions were then implanted into the whiskers with the energy of 60 keV, under the vacuum of 2×10^{-5} mbar and a rough dose of approximately 5×10^{16} ion/cm². After the implantation process, it could be observed that the implanted whiskers changed from transparent to semi-transparent. The Raman spectroscopy using the 514.5 nm Ar⁺ laser with a backscattering optical configuration was then used in order to investigate and compare the characteristics of the implanted and unimplanted whiskers. The orientation of the implanted whiskers and the laser polarization were taken into account for analysis. The electrical conductivity of the whiskers was measured by using the HP E3633A DC power supply and the HP 34970A multimeter at the temperature ranging from 25 to 200 °C. The Hall measurement was also used to explore the electrical concentration of the implanted whiskers in this research.

3. Results and discussion

3.1. Raman spectroscopy analysis

MoO₃ has an orthorhombic crystal structure consisting of double layers of distorted MoO₆ octahedral held together by covalent forces in the *a* and *c*-axis directions and by the weaker Van der Waals forces in the *b*-axis direction. The Mo–O distance of the distorted octahedrons and three inequivalent oxygen atoms—namely O1, O2, and O3, respectively are shown in Fig. 1. The length of the shortest bond is 1.67 Å. This corresponds to the Mo–O1 bond. In the *a*-axis direction, there are two Mo–O3 bonds with the distances of 2.23 Å and 1.73 Å, respectively. There are three bondings between O2 and Mo. Two equal bondings are along the *c*-axis with the distance of 1.95 Å. The third bonding is in the *b* axis direction with the distance of 2.33 Å. The space group is D_{2h}^{16} . There are 16 atoms in a unit cell. Four atoms are molybdenum and the remainders are oxygen. This results in 48 eigenmodes at the center of Brillouin zone ($q = 0$) which can be described by the displacements of the atoms. This could be either parallel or perpendicular to the chain axis *c*. The irreducible representation is given as:

$$\Gamma = 8A_g + 8B_{1g} + 4B_{2g} + 4B_{3g} + 4A_u + 3B_{1u} + 7B_{2u} + 7B_{3u}$$

where A_g, B_{1g}, B_{2g}, and B_{3g} are Raman-active modes, A_u is an inactive mode, and the remainders are infrared-active modes.

Table 1
Raman selection rules for backscattering corresponding to all possible cases

Cases	Scattering configuration	Allowed modes	Tensor components
$k a, E b$	$x(yz)\vec{x}$ $x(yz)\vec{x}$	A_g B_{3g}	α'_{xy} α'_{yz}
$k a, E c$	$x(zx)\vec{x}$ $x(zx)\vec{x}$	A_g B_{3g}	α'_{xz} α'_{yz}
$k b, E a$	$y(xx)\vec{y}$ $y(xz)\vec{y}$	A_g B_{2g}	α'_{xx} α'_{xz}
$k b, E c$	$y(zz)\vec{y}$ $y(zx)\vec{y}$	A_g B_{2g}	α'_{xz} α'_{xz}
$k c, E a$	$z(xx)\vec{z}$ $z(xy)\vec{z}$	A_g B_{1g}	α'_{xx} α'_{xy}
$k c, E b$	$z(yy)\vec{z}$ $z(yz)\vec{z}$	A_g B_{1g}	α'_{yy} α'_{xy}

The Raman tensors corresponding to A_g, B_{1g}, B_{2g}, and B_{3g} are:

$$\begin{pmatrix} \alpha'_{xx} & 0 & 0 \\ 0 & \alpha'_{yy} & 0 \\ 0 & 0 & \alpha'_{zz} \end{pmatrix}, \begin{pmatrix} 0 & \alpha'_{xy} & 0 \\ \alpha'_{xy} & 0 & 0 \\ 0 & 0 & 0 \end{pmatrix}, \begin{pmatrix} 0 & 0 & \alpha'_{xz} \\ 0 & 0 & 0 \\ \alpha'_{xz} & 0 & 0 \end{pmatrix}$$

and $\begin{pmatrix} 0 & 0 & 0 \\ 0 & 0 & \alpha'_{yz} \\ 0 & \alpha'_{yz} & 0 \end{pmatrix}$,

respectively.

These Raman tensors lead to the selection rules for the six cases of our experiment as given in Table 1.

Fig. 2 shows the Raman spectra of the unimplanted MoO₃ whiskers in the frequency range of 60–1100 cm⁻¹. The intensity of the Raman peaks varies based on the crystal orientation and polarization of the laser source. All the Raman peaks observed are in good agreement with that which has been described in the literature [5]. However, some of the Raman peaks observed in this research will be discussed by applying the selection rules derived from Raman tensors and together with the single crystal MoO₃ reported by Py and Maschke [5].

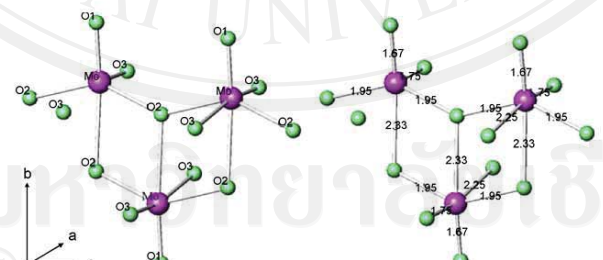


Fig. 1. The crystal structure with labeled atoms and the length of each bond in the crystal structure.

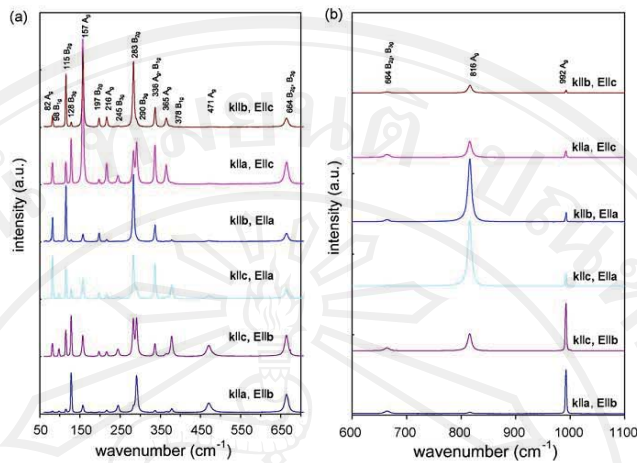


Fig. 2. Raman spectra of unimplanted whiskers taken from six cases of crystal orientation and polarization: (a) 50–700 cm^{-1} and (b) 650–1100 cm^{-1} with the intensity eight times stronger than that in (a).

Three main regions appear for the MoO_3 vibration at 1000–600, 400–200, and below 200 cm^{-1} which correspond respectively to the stretching, deformation, and lattice modes. The Raman peaks at 992 and 816 cm^{-1} are the A_g mode. This corresponds to the $\nu_{\text{as}} \text{Mo}=\text{O}1$ stretching in which the bonding aligns along the b -axis direction and the $\nu_s \text{Mo-O3-Mo}$ stretching in which the bonding aligns along the a axis direction, respectively. This results in a drastically change of intensity when polarization occurs in these directions. The peak at 471 cm^{-1} is the A_g mode which corresponds to the $\nu_{\text{as}} \text{M-O2}$ stretching and bending. This peak appeared only in the case of using polarization aligned along the b -axis direction ($E||b$) and should assign to be the stretching of the 2.33 \AA Mo–O2 bonding. The peak at 378 cm^{-1} is the B_1g mode, corresponding to the $\delta \text{O2-M-O2}$ scissor. As seen in Fig. 2a for the cases of $k||c$ & $E||a$ and $k||c$ & $E||b$, its Raman intensity is maximum in the case of the wave propagates parallel with the c -axis ($k||c$).

The peak at 365 cm^{-1} is the A_g mode and therefore corresponds to the $\delta \text{O2-M-O2}$ scissor. Its Raman intensity is maximum in the case of $E||c$, due to the variation of the angle

between the two 1.95 \AA Mo–O2 bondings lying in the bc plane and also corresponds to the selection rule. The peaks at 283 and 290 cm^{-1} are the B_2g and B_3g modes. This corresponds to the $\delta \text{O1} = \text{M} = \text{O1}$ wagging. The B_2g mode intensity should be higher in the case of $k||b$ than that of other cases whereas the B_3g mode intensity should be higher in the case of $k||a$.

The peak at 157 cm^{-1} is the A_g mode. This corresponds to the $\delta(\text{O}_2\text{Mo}_2)_n$ polyhedron along with the chain axis. Its intensity increased strongly when polarizing along the c -axis direction. The peaks at 82, 98, 115, and 128 cm^{-1} are the A_g , B_1g , B_2g , and B_3g modes, respectively, corresponding to the translational rigid Mo_4 chain mode. The intensity of the A_g peak was at the maximum when polarizing along the a -axis. According to the selection rules, the B_1g , B_2g , and B_3g intensities were at the maximum in the case of $k||c$, $k||b$, and $k||a$, respectively.

Fig. 3a shows examples of the Raman spectra of the implanted MoO_3 whiskers in comparison to that of the unimplanted MoO_3 whiskers. No extra peaks appeared on the entire Raman spectrum of the N^+ implanted whiskers. The

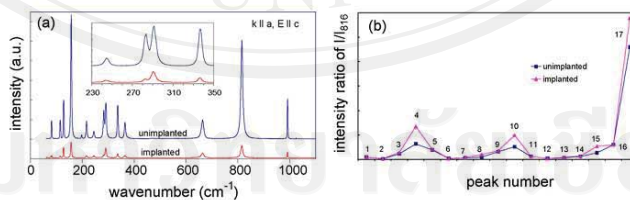


Fig. 3. Raman spectra of implanted and unimplanted whiskers in the case of $k||a$ & $E||c$: (a) 60–1100 cm^{-1} and the inset is an expansion of 230–350 cm^{-1} . (b) The intensity ratio I/I_{416} of the implanted and unimplanted whiskers, where the peaks 1–17 are Raman peaks at 82, 98, 115, ..., and 992 cm^{-1} , respectively where each peak is the summation of the ratio from all six cases.

intensity of these peaks decreased approximately one order of magnitude with respect to that of the unimplanted whiskers. However, in the case of $k||a$ & $E||c$, the inset in Fig. 3a, the I_{290}/I_{283} ratio of the implanted whiskers was approximately 2.5 times higher than that of the unimplanted whiskers. This was determined by using Gaussian curve fitting. The graph in Fig. 3b shows the relative suppressions of the implanted-Raman peaks of the symmetry modes with respect to the A_g symmetry mode at 816 cm^{-1} . From this graph, it can be seen that most of the A_g , B_{1g} , and B_{2g} modes were suppressed with the same ratio whereas all of the B_{3g} modes (see the peaks 4, 8, 10, and 15 in Fig. 3b) were suppressed with a ratio lower than that of the other modes. Therefore, the B_{3g} modes had a higher ratio of I/I_{816} with respect to the unimplanted ratio, which was derived from the case of $k||a$. No other propagation directions have such an observable difference.

The results of Raman intensity decreasing resemble to that of the H^+ ion implantation on a pellet of MoO_3 with a dose lower than 4×10^{16} ions/ cm^2 [4]. This could be explained based on the electronic screening of phonons in the metallic state that the electron transfers from hydrogen to Mo. Therefore, a similar situation could be applied to our results. Dieterle et al. [6] have studied the Raman spectrum of various stoichiometry of MoO_{3-x} . They have found that the ratio of I_{283}/I_{290} decreased linearly as a function of the stoichiometry x , i.e. oxygen vacancy concentration. On the other hand, the distortion due to oxygen vacancy existing in the crystal structure caused the Raman intensity of the B_{3g} mode at 290 cm^{-1} to increase with respect to the B_{2g} mode at 283 cm^{-1} . The comparison between the ratio of I/I_{816} from a single crystal and from polycrystal or film by summing all cases of orientation can be seen in Fig. 3b. This graph suggests that after the implantation, the ratio of I_{283}/I_{290} decreased which was in agreement with what has been observed by Dieterle et al. However, it was worth to summarize that not only the B_{3g} mode at 290 cm^{-1} but all of the B_{3g} modes increased with respect to other modes due to the distortion of the crystal structure from the ion implantation except for the case of $k||a$.

3.2. Electrical properties

In this research, the electrical conductivity (σ) as a function of temperature for the implanted MoO_3 whisker specimens was determined, as shown in Fig. 4. This could be represented by the well known exponential relation:

$$\sigma = A \exp\left(\frac{-E_a}{kT}\right),$$

where A is Arrhenius constants, E_a is the activation energy for the conduction processes, k is the Boltzmann constant and T is the specimen temperature in Kelvin.

From the curve fitting of the data collected from the experiments, the expression above could be written as:

$$\sigma = 3.58 \times 10^{-1} \exp\left(\frac{-0.041\text{ eV}}{kT}\right) \Omega^{-1} \text{ cm}^{-1}.$$

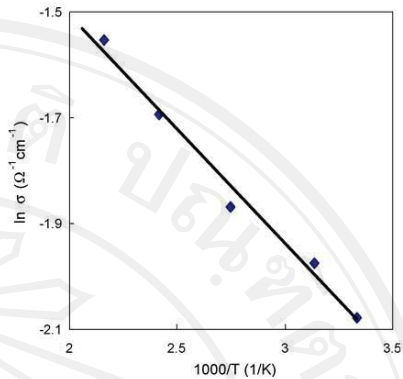


Fig. 4. Electrical conductivity as a function of temperature for the implanted MoO_3 whiskers.

The activation energy of implanted whiskers was about 0.041 eV. The conductivity was enhanced to about $0.074\text{ } \Omega^{-1} \text{ cm}^{-1}$ at a room temperature. This is approximately seven orders of magnitude greater than that of the results from Pandit et al. [10]. From the Hall measurement, the implanted whiskers exhibited as an n-type semiconductor and their electron concentration was about $7 \times 10^{16} \text{ cm}^{-3}$. Pandit et al. reported that MoO_3 exhibits the electrical conductivity differently in two regions of temperature. The higher temperature region was above 380°C for a single crystal. The activation energy of this region was about 1.75 eV which can be referred to as the intrinsic conduction. For the lower temperature region, the activation energy was about 0.05 eV which was in good agreement with our results. This low activation energy can be categorized as the extrinsic conduction due to impurity, point defects or interstitials, which could not be removed easily [11] and often presented in the forbidden gap of the crystal. From the Raman analysis carried out, it could be confirmed that this is due to the nitrogen ions, which was regarded as impurity, inserted into the layer of the MoO_3 structure and did not bond with Mo. In other words, the implantation of nitrogen ions may increase the electrical conductivity by forming a shallow donor which can be referred to as the n-type conductivity.

4. Conclusions

The Raman spectroscopy of N^+ implanted MoO_3 whiskers was characterized and compared with the unimplanted MoO_3 whiskers in various orientations and polarization directions. The electrical conductivity of the implanted whiskers was also measured. The experimental results have shown that the Raman intensities of the implanted MoO_3 whiskers decrease, with respect to that of the unimplanted whiskers, in which the Raman intensity of the B_{3g} modes were suppressed to a ratio lower than other modes by the distortion due to ion implantation. The distinction of suppression ratio was only in the case of the wave propagation parallel to the a -axis. It

could also be observed that the A_g modes were strongly polarized. Moreover, the electrical conductivity of the MoO_3 whiskers was enhanced obviously by the nitrogen ion implantation and the whiskers exhibited as n-type semiconductor with the activation energy of about 0.041 eV.

Acknowledgements

Surachet Phadungdhitidhada is currently supported by the Grants for Development for New Faculty Staff (GDNFS) Scholarship from the Thai government. We would like to thank the Department of Physics, Faculty of Science, Chiang Mai University, Chiang Mai, Thailand for providing access to its ion implantation facility.

References

- [1] C.M. Julien, Lithium intercalated compounds: charge transfer and related properties, *Mater. Sci. Eng.: R* 40 (2003) 47–102.
- [2] K. Bange, Colouration of tungsten oxide films: a model for optically active coatings, *Sol. Energy Mater. Sol. Cells* 58 (1999) 1–131.
- [3] Z. Zhou, K. Kato, T. Komaki, et al., Effects of hydrogen doping through ion implantation on the electrical conductivity of ZnO , *Inter. J. Hydrogen Energy* 29 (2004) 323–327.
- [4] T. Hirata, K. Ishioka, M. Kitajima, Raman spectra of MoO_3 implanted with protons, *Appl. Phys. Lett.* 68 (4) (1996) 458–460.
- [5] M.A. Py, K. Maschke, Intra- and interlayer contributions to the lattice vibrations in MoO_3 , *Physica B* 105 (1981) 370–374.
- [6] M. Dieterle, G. Weinberg, G. Mestl, Raman spectroscopy of MoO_3 . Part I. Structural characterization of oxygen defects in MoO_{3-x} by DR UV/VIS Raman spectroscopy and X-ray diffraction, *Phys. Chem. Chem. Phys.* 4 (2002) 812–821.
- [7] G.-A. Nazri, Far-infrared and Raman studies of orthorhombic MoO_3 single crystal, *Solid State Ionics* 53–56 (1992) 376–382.
- [8] S. Choopun, P. Mangkorntong, P. Subjareon, N. Mangkorntong, et al., Orthorhombic MoO_3 whiskers by vapor transport method, *Jpn. J. Appl. Phys.* 43 (2004) L91–L93.
- [9] T. Vilaitong, D. Suwannakachorn, B. Yotsombat, D. Boonyawan, et al., Ion implantation in Thailand (I)—development of ion implantation facilities, *ASEAN J. Sci. Technol. Devol.* 14 (1997) 87–102.
- [10] A.K. Pandit, M. Prasad, T.H. Ansari, R.A. Singh, B.M. Wanklyn, Electrical conduction in MoO_3 single crystal, *Solid State Commun.* 80 (1991) 125–127.
- [11] M.S. Seltzer, R.I. Jaffee, *Defect and Transport in Oxides*, Plenum Press, New York, 1974, pp. 315–331.

Paper II



Synthesis of MoO₃ nanobelts by medium energy nitrogen ion implantation

Surachet Phadungdhitdhada ^a, Pongsri Mangkorntong ^a, Supab Choopun ^{a,b},
Nikorn Mangkorntong ^a, Duangmanee Wongratantanaphisan ^{a,b,*}

^a Department of Physics and Materials Science, Faculty of Science, Chiang Mai University, Chiang Mai 50200, Thailand

^b ThEP Center, CHE, 328 Si Autthaya Rd., Ratchathewi, Bangkok 10400, Thailand

ARTICLE INFO

Article history:
Received 2 February 2010
Accepted 26 October 2010
Available online xxxx

Keywords:
Ion implantation technique
Nanobelts
MoO₃ whiskers
Vapor-solid mechanism

ABSTRACT

Ion implantation has been revealed as a potential technique to modify the surface of materials. In this work, MoO₃ nanobelts were synthesized on MoO₃ whisker surfaces by means of ion implantation with 60 keV nitrogen ions at a dose of 1×10^{16} atom/cm² and characterized by scanning electron microscopy, Raman spectroscopy, and transmission electron microscopy. The result showed that the nanostructures of MoO₃ occurred over the whisker surfaces and had belt-like shapes. The size of the synthesized MoO₃ nanobelts mostly ranged from 20 to 60 nm in width and 300 to 800 nm in length. The nanobelts were found to have an orthorhombic crystal structure with growth preferential in the [001] direction. The growth process of the nanobelts based on the common vapor-solid mechanism is discussed.

© 2010 Elsevier B.V. All rights reserved.

1. Introduction

In the past decade, much attention has been focused on one-dimensional nanomaterials with different morphologies including nanotubes, nanowires/nanorods and nanobelts because dimensionality plays a crucial factor in understanding the confinement of transport phenomena in functional materials [1] and in determining their properties [2]. One-dimensional nanomaterials have attracted extensive interest for their promising applications as nanodevices, nanosensors, and other electronic applications. Among the different geometries of nanomaterials, nanobelts exhibit distinct properties leading to special applications due to sharp corners and edges. So far, many nanobelts, such as ZnO, CdO, SnO₂, and Si have been synthesized by high temperature processes [2–4].

MoO₃ has many possible applications in electronic display systems, solid state microbatteries, gas sensors, recording materials, and catalysis [5–7]. Moreover, the layered structure of MoO₃ offers rich intercalation chemistry [8]. Recently, many types of MoO₃ nanostructures have been reported [9–14]. Large-area MoO₃ nanowires were prepared on a silicon substrate by heating a Mo boat in vacuum [9,10]. MoO₃ nanorods were synthesized by a hydrothermal route or solution-based method [11,12]. MoO₃ quasi-nanotubes have been prepared on a Ta substrate by infrared irradiation heating in high vacuum [13]. Also, MoO₃ nanospheres were prepared on a Si substrate by electrical heating of a Mo-coil [14].

Nanobelts of MoO₃ can be fabricated by many methods, such as solution-based method [15,16] and high temperature method using metallic molybdenum [17,18]. However their size is rather large, of a few hundred nanometers width. Our previous work has shown that the implantation of nitrogen ions into MoO₃ whiskers can cause defects in the MoO₃ crystal structure leading to drastic change in the electrical properties of MoO₃ whiskers [19]. In this report, we present a method based on ion implantation to synthesize nanobelts of MoO₃ with a small size by using MoO₃ whiskers as the starting material.

2. Experimental

The synthesis was based on medium energy implantation of nitrogen ions into MoO₃ whiskers which were grown by the vapor transport method. A varian ion implanter model 200-DF5 was employed in this experiment. Details regarding the crystal growth technique and identification of the whiskers can be found elsewhere [20]. In general, the ion implantation process is used to implant the required atoms or ions into the matter. In this work, the heat generated inside the whiskers by energetic ions was also important for the growth of nanostructures on the whisker surfaces. For the start, a set of MoO₃ whiskers, 1–2 mm width and ~8 mm long, was attached to an aluminum plate (53 mm × 80 mm × 0.8 mm) by gluing at the both ends of the MoO₃ whiskers with a silver paint. It was then implanted with 60 keV nitrogen ions (N⁺) for 40 min with a final dose of 1×10^{16} atom/cm² under a pressure of 2×10^{-5} mbar. In the process, the aluminum plate was placed vertically onto a holder which made contact with a water cooling system (~16 °C) in the vacuum chamber. The ion beam was controlled to be rectangularly scanning over the entire aluminum plate. After implantation, the whiskers changed their physical features from colorless to soft purple.

* Corresponding author. Department of Physics and Materials Science, Faculty of Science, Chiang Mai University, Chiang Mai 50200, Thailand. Tel.: +66 53 943 375; fax: +66 53 357 511.

E-mail address: surelity@gmail.com (D. Wongratantanaphisan).

A field emission scanning electron microscope [(FE-SEM) JSM-6700F] was used to observe the morphology of the implanted whisker surfaces. Only belt-like nanostructures were found on some parts of the implanted whiskers. Micro Raman spectroscopy using the 514.5 nm line of the Ar⁺ laser with a backscattering optical configuration was then used to characterize the phase structure. The MoO₃ nanobelts were also characterized by a transmission electron microscope [(TEM) JEM-300F].

3. Results and discussion

A lot of nanobelts were found on the whisker surfaces near the silver paint area, as depicted in Fig. 1. The nanobelts had grown and laid randomly on the whisker surfaces near the silver paint area, as shown in Fig. 1a. A high-magnification image of the nanobelts, as seen in Fig. 1b, showed that the nanobelts were smaller than those reported formerly [15–18]. The width ranged from 20 to 60 nm and the length was in the range of 300–800 nm. The density of MoO₃ nanobelts was about 20 nanobelt/μm². A few shorter nanobelts were found on other areas and no nanobelts occurred in the middle of some whiskers. Generally, MoO₃ has two phases of the crystal structure, orthorhombic MoO₃ and monoclinic MoO₃. Raman scattering is a convenient method to verify not only the vibrational spectra but also the crystal phase structure. In MoO₃, there are three well-defined Raman lines that are different in both structure phases [21]. These modes corresponding to the orthorhombic phase occur at 665, 817, and 994 cm^{−1}, whereas those of the monoclinic phase occur at 776, 848, and 902 cm^{−1}. The measured spectra were qualitatively consistent with the previously reported [19]. Fig. 2 shows the Raman spectra of the MoO₃ nanobelts centered at 665, 817, and 994 cm^{−1}. This suggests that the lattice structure of the MoO₃ nanobelts has the pure orthorhombic symmetry.

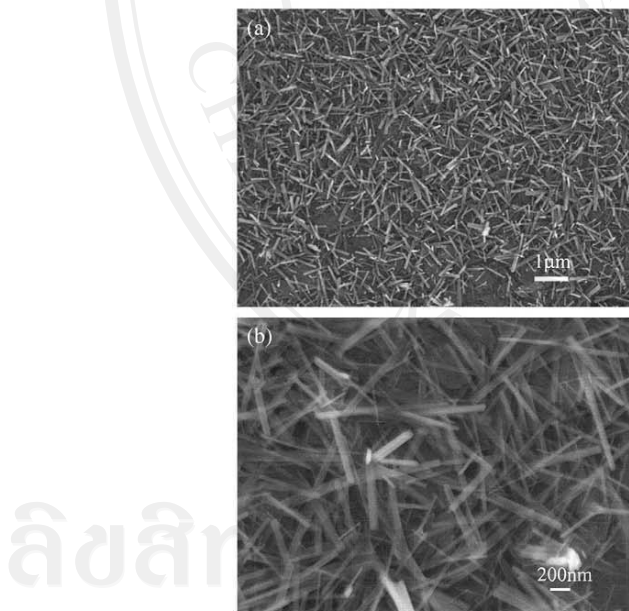


Fig. 1. FE-SEM image of the surface of the N⁺ implanted MoO₃ whisker (a) near the silver area and (b) higher magnification of (a).

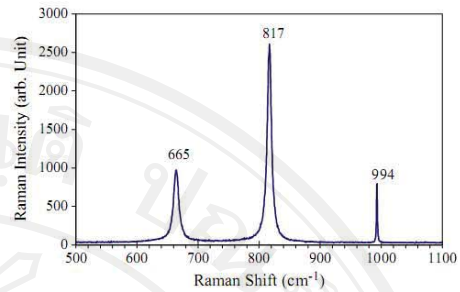


Fig. 2. Representative Raman spectra of MoO₃ nanostructures, showing the pure orthorhombic crystal structure.

The intensity of Raman peak basically depends on the polarizability of the electron cloud of the stretching bond. Therefore, Raman peaks arise with different intensity. The strongest peak was at 817 cm^{−1} which represents the A_g mode. This mode corresponds to the stretching of the Mo–O–Mo bond along the a axis in the crystal structure of the MoO₃, which means that its polarizability is the highest.

Further characterization of the nanobelts was done by TEM operating at 200 kV. A typical TEM image and selected area electron diffraction (SAED) pattern corresponding to the TEM image of the nanobelts are shown in Fig. 3. It revealed that the nanobelt was single crystalline with some polycrystalline impurity indicated by a ring around the central spot of the SAED pattern. The presence of the polycrystalline was probably induced by the penetration of the nitrogen ions during the implantation. The nanobelts have grown in the longitudinal direction lying along the [001] direction of the orthorhombic MoO₃, similar to previously reported [15–18].

MoO₃ nanobelt synthesis reported so far were processed through either the hydrothermal route method [15,16] or a high temperature method [17,18]. For the high temperature method, metallic molybdenum was heated in atmosphere under flowing argon/oxygen gas. The metallic oxide was evaporated from the metallic source at a high temperature region and then drifted to deposit onto a substrate at a lower temperature region. Results showed that the size of the nanobelts was in the order of a few hundred nanometers in width [17,18]. This method is similar to the vapor transport method in which the growth mechanism of the MoO₃ crystals is based on the vapor-solid (VS)

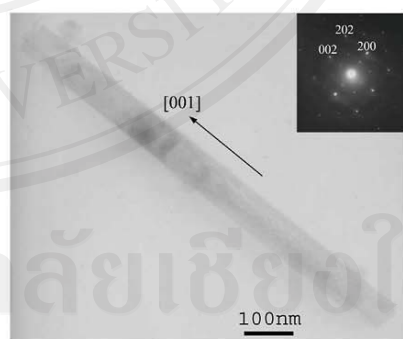


Fig. 3. Representative TEM image of the MoO₃ nanobelt. Inset shows the corresponding SAED pattern taken with the incident beam in the [010] direction.

mechanism. In the VS mechanism, the size of MoO_3 crystals is proportional to time and growth rate which depend on evaporation rate and system pressure. Theoretically, the formation of wire/belt-like nanostructures can be explained by the kinetics of crystal growth via the 2D nucleation probability [22] which is expressed as

$$P_N = B \exp \left(- \frac{\pi \sigma^2}{k^2 T^2 \ln(\alpha)} \right) \quad (1)$$

where P_N is a nucleation probability, B is a constant, σ is the surface energy of the solid whisker, k is the Boltzmann constant, T is the absolute temperature, and α is the supersaturation ratio defined as $\alpha = p/p_0$, where p is vapor pressure and p_0 is the equilibrium vapor pressure corresponding to temperature T . A higher temperature and larger supersaturation ratio lead to a sheet-like structure. In comparison, lower temperature and smaller supersaturation ratio promote the growth of a wire/belt-like structure. The evaporation rate and the system pressure could have effect on the growth via the vapor pressure in terms of the supersaturation ratio as seen in the 2D nucleation probability equation. To reduce these parameters, this work dealt with ion implantation which used a penetrated ion as a very small local heater to evaporate MoO_3 out from the whiskers for the growth of nanostructures.

During the ion implantation process, each nitrogen ion carried an energy of 60 keV to hit the whiskers and the aluminum plate. By using the Transport of Ion in Matter (TRIM) program [23] to calculate the energy of the nitrogen ions loss in the MoO_3 matter, about 65% of the energy was used to ionize atoms in the target and then changed into heat energy when the atoms returned to their original status, while the remaining energy was used to generate phonons. However, it was hard to estimate the temperature in MoO_3 whiskers. Therefore, the temperature in the aluminum plate was estimated. Then the level of the temperature in the MoO_3 whiskers could be approximated as higher than the temperature in the aluminum plate because the MoO_3 whiskers have a lower heat capacity and were bombarded with the same amount of nitrogen ions per unit area as the aluminum plate. Under unrigorous calculation based on the bombardment of the 60 keV nitrogen ions about $2 \times 10^{12} \text{ ion/cm}^2 \text{ s}$ onto the aluminum plate ($53 \text{ mm} \times 80 \text{ mm} \times 0.8 \text{ mm}$), the temperature in the aluminum plates was expected to rise to about 500°C at the end of the implantation process with a temperature rate of 0.21°C/s . Certainly, the actual temperature of the aluminum plates should be lower than this temperature because some of the heat should transfer to the holder and the water cooling system. Therefore, the temperature of the MoO_3 whiskers could be higher than 500°C . The sublimation point of MoO_3 is about 700°C [24] but MoO_3 could sublime at a lower temperature in vacuum, so that the actual temperature of the MoO_3 whiskers was high enough to evaporate them. In this ion implantation process, nitrogen ions penetrated into the MoO_3 whiskers to a depth of about 240 nm and its maximum concentration occurred at a depth of about 110 nm, both calculated by the TRIM program. Hence the hottest point was 110 nm inside the whiskers. Vapor was generated inside the whiskers with a low evaporation rate and then flowed out to condense at a lower temperature near the whisker surfaces as depicted in Fig. 4. Since there was a large pressure difference between the vapor source inside the whiskers and the whisker surfaces, some of the vapor could flow quickly into the vacuum when it was generated. Hence, MoO_3 crystals gradually formed with the VS mechanism to be MoO_3 nanostructures. Since the MoO_3 crystals have an orthorhombic structure with the lattice parameter: $a = 3.96 \text{ \AA}$, $b = 13.86 \text{ \AA}$, and $c = 3.70 \text{ \AA}$, it should be grown preferentially in the c direction due to a lowest surface energy of the (001) plane and belt-like structure should be formed due to large differences in the close-packing rate among the (100) and (010) planes. As mentioned, at the regions near the silver paint area, the

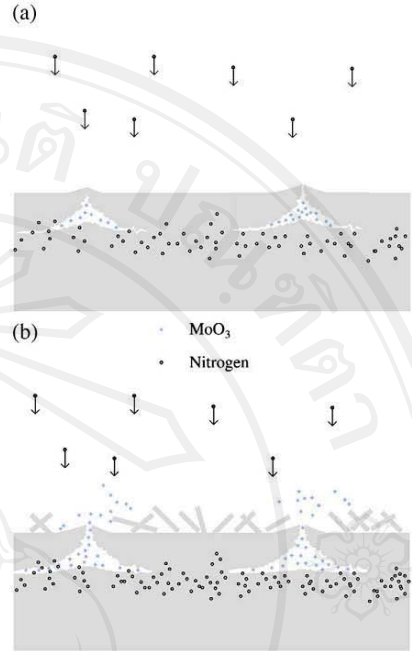


Fig. 4. The purposed growth process of MoO_3 nanobelts: (a) starting crack due to high vapor pressure and (b) formation of the MoO_3 vapor on the surface.

denser and longer nanobelts were observed because these regions were better attached to the aluminum plate and had a lower temperature than the middle part of the whiskers. The nanobelts could not be grown at the middle of some whiskers as the temperature of those parts was too high, leading to the re-evaporation effect.

The MoO_3 nanobelts are also useful in many applications such as a cathode material for rechargeable lithium batteries which requires a layer structure material. This method offers a technique to modify the surface of MoO_3 whiskers by growing the MoO_3 nanobelts. It could potentially be manipulated to MoO_3 thick films in further applications.

4. Conclusion

In conclusion, small size nanobelts of MoO_3 were successfully synthesized on the MoO_3 whiskers by an ion implantation technique. The ion implantation can be regarded as a small heater placed inside the whiskers. The vapor was generated inside the whiskers and then flowed out to condense at the whisker surfaces forming MoO_3 nanobelts based on the VS mechanism. The synthesized MoO_3 nanobelts have an orthorhombic symmetry with preferential growth in the [001] direction. The sizes of the nanobelts ranged from 20 to 60 nm in width and 300 to 800 nm in length.

Acknowledgments

This work was supported by the NANOTEC, NSTDA, Ministry of Science and Technology, Thailand, through its program of Center of Excellence Network and the Graduate School, Chiang Mai University.

Thailand. Surachet Phadungdhitidhada was supported by the Grants for Development for New Faculty Staff (GDNFS) Scholarship from the Thai government. We would like to thank the Department of Physics and Materials Science, Faculty of Science, Chiang Mai University, Chiang Mai, Thailand for providing access to its ion implantation facility.

References

- [1] Pan ZW, Dai ZR, Wang ZL. Science 2001;291:1947–9.
- [2] Hu J, Odom TW, Lieber CM. Acc Chem Res 1999;32:435–45.
- [3] Dai ZR, Gole JL, Stoum JD, Wang ZL. J Phys Chem B 2002;106:1274–9.
- [4] Shi W, Peng H, Wang N, et al. J Am Chem Soc 2001;123:11095–6.
- [5] Hsain Z. J Mater Res 2001;16:2695–708.
- [6] Ferroni M, Guidi V, Martinelli G, Sacerdoti P, Nelli P, Sberveglieri G. Sens Actuators B 1998;48:285–8.
- [7] Zeng HC. Inorg Chem 1998;37:1967–73.
- [8] Zeng HC, Xie F, Wong KC, Mitchell KAR. Chem Mater 2002;14:1788–96.
- [9] Zhou J, Xu NS, Deng SZ, Chen J, She JC, Wang ZL. Adv Mater 2003;15:1835–40.
- [10] Zhou J, Deng SZ, Xu NS, Chen J, She JC. Appl Phys Lett 2003;83:2653–5.
- [11] Lou XW, Zeng HC. Chem Mater 2002;14:4781–9.
- [12] Wen Z, Wang Q, Li J. J Nanosci Nanotechnol 2006;6:2117–22.
- [13] Li Y, Bando Y. Chem Phys Lett 2002;364:485–8.
- [14] Zhao Y, Liu J, Zhou Y, Zhang Z, Xu Y, Naramoto H, Yamamoto S. J Phys Condens Matter 2003;15:1547–52.
- [15] Li XL, Liu JF, Li YD. Appl Phys Lett 2002;81:4832–4.
- [16] Wang S, Zhang Y, Ma X, Wang W, Li X, Zhang Z, Qian Y. Solid State Commun 2005;136:283–7.
- [17] Li YB, Bando Y, Golberg D, Kurashima K. Appl Phys Lett 2002;81:5048–50.
- [18] Siciliano T, Tepore A, Filippo E, Micocci G, Tepore M. Mater Chem Phys 2009;114:687–91.
- [19] Phadungdhitidhada S, Mangkornton P, Choopun S, Mangkornpong N. Ceram Int 2008;34:1121–5.
- [20] Choopun S, Mangkornpong P, Subjareon P, Mangkornpong N, Tabata H, Kawai T. Jpn J Appl Phys 2004;43:L91–3.
- [21] Seguin L, Figlarz M, Cavagnat R, Lassegues JC. Spectrochimica Acta Part A 1995;51:1323–44.
- [22] Dai ZR, Pan ZW, Wang ZL. Adv Funct Mater 2003;13:9–24.
- [23] <http://www.srim.org>.
- [24] Lewis RJ. Hawley's Condensed Chemical Dictionary. 14th ed. New York: John Wiley & Sons; 2001.

Paper III

SnO₂ nanowires mixed nanodendrites for high ethanol sensor response

Surachet Phadungdhitdhada¹, Suvit Thanasanvorakun², Pongsri Mangkorntong¹, Supab Choopun^{1,3}, Nikorn Mangkorntong¹, and Duangmanee Wongratanaaphisan^{1,3}

¹Department of Physics and Materials Science, Faculty of Science, Chiang Mai University, Chiang Mai 50200, Thailand.

²Faculty of science and Agriculture Technology, Rajamangala University of Technology Lanna, Chiang Mai Campus, Chiang Mai, Thailand.

³Thailand Center of Excellent in Physics, CHE, 328 Si Autthaya Rd., Ratchathewi, Bangkok 10400, Thailand.

Corresponding author. E-mail: dwongrat@chiangmai.ac.th ; Fax: +66-53 357 511

Tel.: +66-53 943 375

Abstract

Mixed morphology of SnO₂ nanowires and nanodendrites was synthesized on the gold-coated alumina substrates by carbothermal reduction of SnO₂ in closed crucible. The products were characterized by scanning electron microscopy, x-ray diffractometer, and transmission electron microscopy. Results showed the SnO₂ nanowires and the SnO₂ nanodendrites branched out from the main nanowires. Both SnO₂ nanostructures were pure tetragonal rutile structure. The nanowires were grown in [101] and [121] directions with the diameter of 50–150 nm and the length of a few

ten micrometers. The nanodendrites were about 100–300 nm in diameter. The growth mechanism of the SnO_2 nanostructures was also discussed. Characterization of ethanol gas sensor, based on the mixed morphology of the SnO_2 nanostructures, was carried out. The optimal temperature was about 360°C and the sensor response was 120 for 1000 ppm of ethanol concentration.

Keywords: carbothermal reduction, ethanol gas sensor, SnO_2 nanowires, SnO_2 nanodendrites

1. Introduction

Metal oxide nanostructured materials have been revealed a great step to functionalize materials with high surface to volume ratio, leading to enormous effective applications such as gas sensors [1], transparent conductors [2], electrochemical energy storages [3], solar cells [4] etc. Morphology of these nanomaterials is also a factor to control their properties. Noticeable in recent years, intensive researches have been focusing on nanomaterials with controllable size and shape to step toward for addition of applications and realization of functional nanosystems [1, 4, 5]. For such applications, SnO_2 (3.6 eV bandgap n-type semiconductor) is one of the rapidly growing interests. So far various shapes of SnO_2 nanostructures have been prepared by employing different techniques. For example, flower-like, prism-like, cubic-like, nanosheet, and hollow sphere SnO_2 nanostructures have been synthesized by hydrothermal route [6–9]. SnO_2 nanowires/nanobelts have also been synthesized mostly by thermal oxidation [10, 11].

or thermal evaporation including carbothermal reduction [12–17] and vapor phase transport [18, 19]. SnO_2 nanotubes have been synthesized using various techniques such as electrospinning and atomic layer deposition [20], sol gel–template [21], electrochemical [22], etc. However, methods or techniques to synthesize various morphologies of the SnO_2 nanostructures, especially three dimension (3D) nanostructures, still open for challenge.

In gas sensor applications, gas sensors based on various morphologies of the SnO_2 nanostructures have widely been investigated [7, 12–17]. It was suggested that gas sensing properties strongly depend on the morphology of SnO_2 . The mixed morphology among the SnO_2 nanostructures is promising to a unique gas sensing performance which is required to improve the performance of the e–nose. By this contribution, we report a carbothermal reduction technique to synthesize the mixed morphology of SnO_2 nanowires and nanodendrites. In addition, the ethanol gas sensing properties of such mixed morphology were characterized.

2. Experimental

2.1 Synthesis of SnO_2 nanostructures

Firstly, powder of SnO_2 and carbon, with a weight ratio of 1:5, was mixed mechanically in a mortar for one hour. Then, 0.1g of the mixture was screened dispersedly at bottom of a crucible and Au–coated alumina substrates were placed in the crucible above the mixture. The crucible, closed with a lid and tightened by covering with aluminum foil, was placed into a horizontal alumina tubular furnace at room temperature. The furnace was then heated to 850°C and kept at this temperature

for an hour. Finally, the crucible was moved out after the furnace was cool down to room temperature. In the crucible, thick white wool-like layer covered over surface of the alumina substrates and a few microwhiskers were found on the crucible wall. The morphology and structure of the product were characterized by employing field emission scanning electron microscopy (FE-SEM, JSM-6700F) and transmission electron microscopy (TEM, JEM-300F). The crystal structure and the phase purity of the product were identified by x-ray diffractometer (XRD, Cu K α radiation with $\lambda=0.1542$ nm).

2.2 Preparation of sensors

In order to make sensors based on the synthesized SnO₂ nanostructures, the white wool-like layer of the SnO₂ nanostructures was flatten by dropping ethanol and dried at 100°C to remove the ethanol. Then, a gold electrode was made on the film of the SnO₂ nanostructures by using gold paste and the obtained sensor was connected to an electronic circuit for gas sensing characterization. Ethanol sensing performance was carried out through a gas-confined chamber with inlet and outlet. 1 ml/min air flow was fed into the chamber as a reference gas through the inlet. The inlet was switched between air and air + ethanol vapor for turning on/off ethanol vapor gas. The sensors were tested with ethanol vapor gas of 50, 100, 200, 500, and 1000 ppm at the operating temperature of 260–380°C. The ethanol vapor with various concentrations was generated from ethanol solution at 34°C in the ethanol breath simulator (GUTH laboratory Inc., Harrisburg USA) which simulated the alcohol concentration in exhaled human breath. The responses of the sensors to the ethanol vapor gas were measured using a volt–amperometric technique. The gas sensor

response (S) was defined as the ratio of the electrical resistance in air to that in the explosion of gas, R_{air}/R_g .

3. Result and discussion

3.1 Characterization of SnO_2 nanostructures

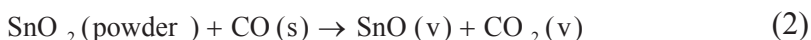
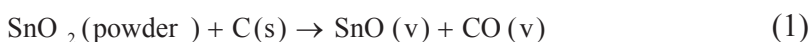
Typical SEM images presenting morphologies of the as-synthesized SnO_2 products are shown in Fig. 1. Fig. 1a and Fig. 1b show overview of the products in low magnification and in higher magnification, respectively. It revealed that the white wool product was SnO_2 nanostructure layer of ultra long nanowires decorated with fuzzy branches. The SnO_2 nanowires laid randomly on the substrate. The SnO_2 nanowires have the diameter of 50–150 nm with only a few ones in the diameter up to 1 μm and the length of a few ten micrometers. These fuzzy branches could be called “nanodendrites” which are meandering chains with random branches. The inset in Fig. 1b shows the linkages of these random branches from two different SnO_2 nanowires. The length of the SnO_2 nanodendrites was a few micrometers. These evidences indicated that the nanowires were formed firstly and the nanodendrites come to attach on the nanowires later.

The XRD pattern of the SnO_2 nanostructures, taken from 20–80 degree of 2θ , is shown in Fig. 2. The pattern can be indexed according to the cassiterite structure of SnO_2 with lattice constants of $a = 4.738 \text{ \AA}$ and $c = 3.187 \text{ \AA}$ (JCPDS 41–1445) and the corundum structure of Al_2O_3 (JCPDS 42–1468) which comes from the substrate. No

impurities were detected in the product. It means that the SnO_2 nanostructures were pure tetragonal rutile structure.

Under the layer of the mixed morphology, only nanowires were found. These products were then further analyzed using TEM and selected area electron diffraction (SAED). Fig. 3a shows a typical TEM bright field image of the SnO_2 nanowires. The SnO_2 nanowires had a uniform diameter along their entire length. The SAED patterns were randomly taken from the SnO_2 nanowires in Fig. 3a, as shown in Fig. 3b and 3c. The SAED patterns in Fig. 3b and 3c, taken from the above and below dash-line square block in Fig. 3a respectively, indicate that the SnO_2 nanowires preferentially grow along $[10\bar{1}]$ and $[1\bar{2}\bar{1}]$ directions, respectively. The TEM images are shown in Fig. 4 revealing the connection between a nanodendrite and a nanowire. Nanoparticles were attached together randomly forming a nanodendrite. The diameter of nanodendrites was about particle size. The sizes of the nanoparticles attaching at the nanowire were about 200–300 nm. In contrast, the nanoparticles at an end of a nanodendrite were about 100 nm. The SAED pattern of the nanoparticles was taken from the middle of the nanodendrite as shown in the inset of Fig. 4b. The superimposed diffraction pattern around the main spot suggests that the nanoparticles exhibit crystalline structures.

Generally, the synthesis of SnO_2 nanostructures from carbothermal reduction process could be explained by using the following chemical reactions:





The reduction (1) and (2) can be explained by Ellingham diagram which is the plot of standard free energies for formation of oxides versus temperature [23]. The reaction incident of SnO_2 powder to SnO vapor by carbon can occur at above 700°C . Then, the CO product from the reaction (1) further reduces the SnO_2 powder as the reaction (2). The SnO (v) is metastable and will decompose to SnO_2 (s) and Sn (l) as reaction (3) [24]. Moreover, the SnO vapor possibly reacts with oxygen in the system to form SnO_2 (s). The Sn (l) can be oxidized to form SnO (v). It is also possible that the SnO_2 product can be reduced again as the reaction (1) and (2). These reactions will keep cycling until no C or CO in the system.

Considering the reaction in the loosely closed crucible system, the reductions of the SnO_2 powder occurred gradually at the bottom of the crucible when approaching 700°C and were violent when reaching 850°C . The SnO , CO , and CO_2 , which were the gaseous products from the reductions of the SnO_2 powder, soared to the space above the SnO_2+C mixture and substrates. The SnO_2 product, resulting from the decomposition of the SnO (v), could be absorbed by gold droplets on the alumina substrate, leading to the formation of the SnO_2 nanowires with vapor–liquid–solid (VLS) mechanism. Therefore, the SnO_2 nanowires were grown in epitaxial directions, depending on the orientation of the seed crystal. Hence, both $[10\bar{1}]$ and $[1\bar{2}\bar{1}]$ directions were observed. From our results, the SnO_2 nanowires decorated with the SnO_2 nanodendrites. Interesting, the mixed morphology can be achieved by utilizing the oxygen content in the system. Furthermore, for insufficiency of oxygen, SnO_2 crystals grew with no preferential direction, resulting in dendritic crystal [19]. In

comparison with our work on the mixed morphology, the SnO_2 nanowires would initially grew at early period that oxygen was adequate for the oxidation of the SnO (v) or Sn (l). The decrease of oxygen content due to the oxidation reaction and the leakage from high pressure of CO_2 leads to the insufficiency of the oxygen for the oxidation. Therefore, the SnO (v) or Sn (l) had more chance for aggregation to form particles before oxidation. The SnO or Sn particles fell to adhere randomly on the main SnO_2 nanowires. The SnO and Sn particles then gradually oxidized to be SnO_2 particles later. Consequently, the SnO_2 nanodendrites could branch out from the main SnO_2 nanowires.

In the case more oxygen allowed to diffuse into the chamber, only microwires and microbelts were found and no dendritic crystal. With closed system, amount of the oxygen is limited and CO_2 is confined in the system, acting as ambient gas to decrease the growth rate of the SnO_2 crystals. It is worth mentioning that the closed system could be important for the growth of the mixed morphology of the nanostructures.

3.2 Ethanol sensing properties

In order to remove humidity and substances coming with gold paste, the sensors, based on the mixed morphology of the SnO_2 nanowires and nanodendrites, were baked at 300°C before testing. The sensor response was periodically checked during the baking. It was found that the sensor response gradually increased with baking time and saturated at about seven days. The response of a typical sensor as a function of the operating temperatures is shown in Fig. 5. The increase of the sensor response with increasing of temperature reached the optimal temperature at about

360°C. The highest sensor responses for 50, 100, 200, 500, 1000 ppm of ethanol concentration were 22, 31, 53, 83, and 120, respectively.

The sensor response in this work was slightly higher than that of the SnO₂ nanowires [16, 25–27] and the SnO₂ nanoparticles [28], as shown in Fig. 6. Moreover, the operating temperature was in the middle of that of both SnO₂ nanowires [16, 25–27] and SnO₂ nanoparticles [17, 28, 29], which were above 400°C and under 300°C, respectively. To explain the improvement of the sensor response, the gas sensing mechanism of metal oxides semiconductor was intensively investigated.

The gas sensing mechanism of metal oxides has been clarified in previous works [30, 31]. At high temperature, the resistance of the sensing layer changes by adsorption and desorption of oxygen on the surface of the sensing layer. The carrier electrons are consumed by the formation of O[−] and/or O^{2−} and this results in creation of the depletion region on the surface leading to a high potential barrier at the inter-grain. Hongsith et al. [30] have formulated a relation which explains the sensor response of the metal oxide gas sensors in functions of gas concentration, catalytic effect, and nanostructure effect, which can be expressed as

$$S = \left(\frac{\Gamma_t k_{\text{Eth}}(T) (\sigma_0 \Phi (V_m / V_s))^b}{n_0} \right) \frac{D^2}{(D - 2L_d)^2} C^b + 1 \quad (1)$$

where Γ_t is a time constant, $k_{\text{Eth}}(T)$ is the reaction rate constant, σ_0 is a number of oxygen ion per unit area, Φ is a ratio of surface area per volume of material (V_m), V_s is the system volume, n_0 is the electron carrier concentration of the sensor, D is

diameter of nanowire, L_d is the Debye length indicating the depletion layer, C is gas concentration, and b can be referred to the adsorbed oxygen species on the metal oxide surface. The b – value close to 1 (0.5), the surface dominates by O^- (O^{2-}). Our sensor based on SnO_2 mixed morphology, however, could have similar gas sensing mechanism as discussed above.

As seen in sensor response formula, the nanostructures can improve the sensor response in terms of the depletion layer effect and the surface to volume ratio. The average diameters of nanowires and nanoparticles, in this work, were about 90 and 160 nm, whereas the $2L_d$ of SnO_2 is estimated about 30 nm at 360°C [31]. Hence, the sensor response could not be governed by the effect of the depletion layer. Therefore, the improvement of the sensor response in this work, comparing to that of SnO_2 nanowires, could be attributed to the presence of the nanodendrites which increase the surface to volume ratio, resulting in the enhancement of the adsorbed oxygen ion on the nanowire surface.

From the sensor response formula, the b – value can be determined by plotting $\log (S-1)$ against $\log (C)$. The plot is shown in Fig. 7 and fitted with linear relation. It showed a good linear relationship between $\log (S-1)$ and $\log (C)$ with 0.997 of R-squared. The b – value was 0.59, which suggested that the surface of the sensor dominated by O^{2-} at 360°C.

The response time was in the range of 1 – 10 second. The recovery time ranged from several ten to several hundred seconds. The mixed morphology of this work showed a gas sensing performance differing from a morphology of both

nanoparticles and nanowires. Thus, this may lead to an important implication for a development of e–nose based on mixed morphology of oxide semiconductors.

4. Conclusion

Mixed morphology of SnO_2 nanowires and nanodendrites was successfully synthesized by carbothermal reduction of SnO_2 powder. The diameters of the synthesized SnO_2 nanowires and SnO_2 nanodendrites were about 50–150 nm and 100–300 nm, respectively. These SnO_2 nanostructures had a tetragonal rutile structure. The formation of the SnO_2 nanodendrites could be induced by the insufficiency of oxygen content in the system. The sensor response of the mixed morphology was slightly higher than that of the pure nanowires. The improvement of the sensor response was due to the presence of the mixed nanodendrites, causing the enhancement of the surface to volume ratio as indicated in the sensor response formula.

Acknowledgements

This work was supported by the NANOTEC, NSTDA, Ministry of Science and Technology, Thailand, through its program of Center of Excellence Network and the Graduate School, Chiang Mai University, Thailand. Surachet Phadungdhitidhada was supported by the Grants for Development for New Faculty Staff (GDNFS) Scholarship from the Thai government.

References

- [1] S. Choopun, N. Hongsith, P. Mangkorntong, and N. Mangkorntong, Zinc oxide nanobelts by sputtering for ethanol sensor, *Physica E Low Dimens. Syst. Nanostruct.* 39 (2007) 53–56.
- [2] J. C. Manifacier, Thin metallic oxides as transparent conductors, *Thin solid films* 90 (1982) 297–308.
- [3] H. W. Jung and Y. U. Jeong, Electrochemical properties of various transition metal oxides for energy storage, *Stud. Surf. Sci. Catal.* 159 (2006) 633–636.
- [4] S. Choopun, A. Tubitmtae, T. Santhaveesuk, S. Nilphai, E. Wongrat, and N. Hongsith, Zinc oxide nanostructures for application as ethanol sensors and dye–sensitized solar cells, *Appl. Surf. Sci.* 256 (2009) 998–1002.
- [5] S. Phadungdhitidhada, P. Mangkorntong, S. Choopun, N. Mangkorntong, and D. Wongratanaaphisan, Synthesis of MoO_3 nanobelts by medium energy nitrogen ion implantation, *Mater. Lett.* 65 (2011) 568-571.
- [6] Z. Li, X. Li, X. Zhang, and Y. Qian, Hydrothermal synthesis and characterization of novel flower-like zinc-doped SnO_2 nanocrystals, *J. Cryst. Growth* 291 (2006) 258–261.
- [7] A. A. Firooz, A. R. Mahjoub, and A. A. Khodadadi, Highly sensitive CO and ethanol nanoflower-like SnO_2 sensor among various morphologies obtained by using single and mixed ionic surfactant templates, *Sens. Actuators B* 141 (2009) 89–96.
- [8] Y. Li, Y. Guo, R. Tan, P. Cui, Y. Li, and W. Song, Synthesis of SnO_2 nano-sheets by a template-free hydrothermal method, *Mater. Lett.* 63 (2009) 2085–2088.

[9] Y. Li, Y. Q. Guo, R. Q. Tan, P. Cui, Y. Li, and W. J. Song, Selective synthesis of SnO_2 hollow microspheres and nano-sheets via a hydrothermal route, *Chinese Sci. Bull.* 55 (2010) 581–587.

[10] S. Park, C. Hong, J. Kang, N. Cho, and C. Lee, Growth of SnO_2 nanowires by thermal evaporation on Au-coated Si substrates, *Current Appl. Phys.* 9 (2009) s230–s233.

[11] X.L. Ma, Y. Li, and Y.L. Zhu, Growth mode of the SnO_2 nanobelts synthesized by rapid oxidation, *Chem. Phys. Lett.* 376 (2003) 794–798.

[12] A. A. Firooz, A. R. Mahjoub, and A. A. Khodadadi, Highly sensitive CO and ethanol nanoflower-like SnO_2 sensor among various morphologies obtained by using single and mixed ionic surfactant templates, *Sens. Actuators B*, 141 (2009) 89–96.

[13] Z. Ying, Q. Wan, Z. T. Song, and S. L. Feng, SnO_2 nanowiskers and their ethanol sensing characteristics, *Nanotechnology*, 15 (2004) 1682–1684.

[14] J. P. Ge, J. Wang, H. X. Zhang, X. Wang, Q. Peng, and Y. D. Li, High ethanol sensitive SnO_2 microspheres, *Sens. Actuators B*, 113 (2006) 937–943.

[15] J. H. Lee, Gas sensors using hierarchical and hollow oxide nanostructures: Overview, *Sens. Actuators B*, 140 (2009) 319–335.

[16] N. V. Hieu, H. R. Yim, B.K. Ju, and J.H. Lee, Enhanced performance of SnO_2 nanowires ethanol sensor by functionalizing with La_2O_3 , *Sens. Actuator B* 133 (2008) 228–234.

[17] H.C. Chiu and C.S. Yeh, Hydrothermal synthesis of SnO_2 nanoparticles and their gas sensing of alcohol, *J. Phys. Chem. C* 111 (2007) 7256–7259.

[18] D. Calestani, M. Zha, G. Salviati, L. Lazzarini, and L. Zanotti, Nucleation and growth of SnO_2 nanowires, *J. Cryst. Growth*, 275 (2005) e2083–e2087.

[19] A. A. Zhukova, M. N. Rumyantseva, I. A. Petukhov, F. M. Spiridonov, J. Arbiol, and A. M. Gaskov, Effect of oxygen partial pressure on SnO_2 whisker growth, *Inorg. Mater.* 44 (2008) 268–271.

[20] W.S. Kim, B.S. Lee, D.H. Kim, H.C. Kim, W.R. Yu, and S.H. Hong, SnO_2 nanotubes fabricated using electrospinning and atomic layer deposition and their gas sensing performance, *Nanotechnology* 21 (2010) 245605.

[21] G.X. Wang, J.S. Park, M.S. Park, and X.L. Gou, Synthesis and high gas sensitivity of tin oxide nanotubes, *Sens. Actuators B* 131 (2008) 313–317.

[22] M. Lai, J.H. Lim, S. Mubeen, Y. Rheem, A. Mulchamdam, M. A. Deshusses, and N. V. Myung, Size-controlled electrochemical synthesis and properties of SnO_2 nanotubes, *Nanotechnology* 20 (2009) 185602.

[23] http://www.doitpoms.ac.uk/tplib/ellingham_diagrams/index.php, 25 August 2010.

[24] J. Q. Hu, X. L. Ma, N. G. Shang, Z. Y. Xie, N. B. Wong, C. S. Lee, and S. T. Lee, Large-scale rapid oxidation synthesis of SnO_2 nanoribbons, *J. Phys. Chem. B* 106 (2002) 3823–3826.

[25] H. Li, J. Xu, Y. Zhu, X. Chen, and Q. Xiang, Enhanced gas sensing by assembling Pd nanoparticles onto the surface of SnO_2 nanowires, *Talanta* 82 (2010) 458–463.

[26] I.S. Hwang, E.B. Lee, S.J. Kim, J.K. Choi, J.H. Cha, H. J. Lee, B. K. Ju, and J. H. Lee, Gas sensing properties of SnO_2 nanowires on micro-heater, *Sens. Actuators B* (In press, 2009).

[27] N. V. Hieu, Highly reproducible synthesis of very large-scale tin oxide nanowires used for screen-printed gas sensor, *Sens. Actuators B* 144 (2010) 425–431.

[28] J. Zhang, S. Wang, Y. Wang, M. Xu, H. Xia, S. Zhang, W. Huang, X. Guo, and S. Wu, Facile synthesis of highly ethanol-sensitive SnO_2 nanoparticles, *Sens. Actuators B* 139 (2009) 369–374.

[29] L. Xi, D. Qian, X. Tang, and C. Chen, High surface area SnO_2 nanoparticles: Synthesis and gas sensing properties, *Mater. Chem. Phys.* 108 (2008) 232–236.

[30] N. Hongsith, E. Wongrat, T. Kerdcharoen, and S. Choopun, Sensor response formula for sensor based on ZnO nanostructures, *Sens. Actuators B* 144 (2010) 67–72.

[31] N. Barsan and U. Weimar, Conduction model of metal oxide gas sensor, *J. Electroceram.* 7 (2001) 143–167.

Figure captions

Fig. 1. Typical SEM images of the synthesized SnO_2 nanostructures: (a) overview image with low magnification and (b) higher magnification image with the insets showing linkages of nanodendrites.

Fig. 2. XRD profile of the SnO_2 nanostructures.

Fig. 3. TEM image and SAED patterns of the SnO_2 nanowires without nanodendrites.

Fig. 4. TEM images and SAED of the SnO₂ nanodendrites showing (a) linkage of a nanodendrite and a nanowire and (b) a nanodendrite departed from a nanowire.

Fig. 5. The sensor response versus the operating temperature under the ethanol concentration of 50, 100, 200, 500, and 1000 ppm.

Fig. 6. The sensor response against the diameter of nanowires and nanoparticles, corresponding to 100 ppm of ethanol vapor.

Fig. 7. The sensor response -1 against the ethanol concentration at 360°C in logarithm scale.

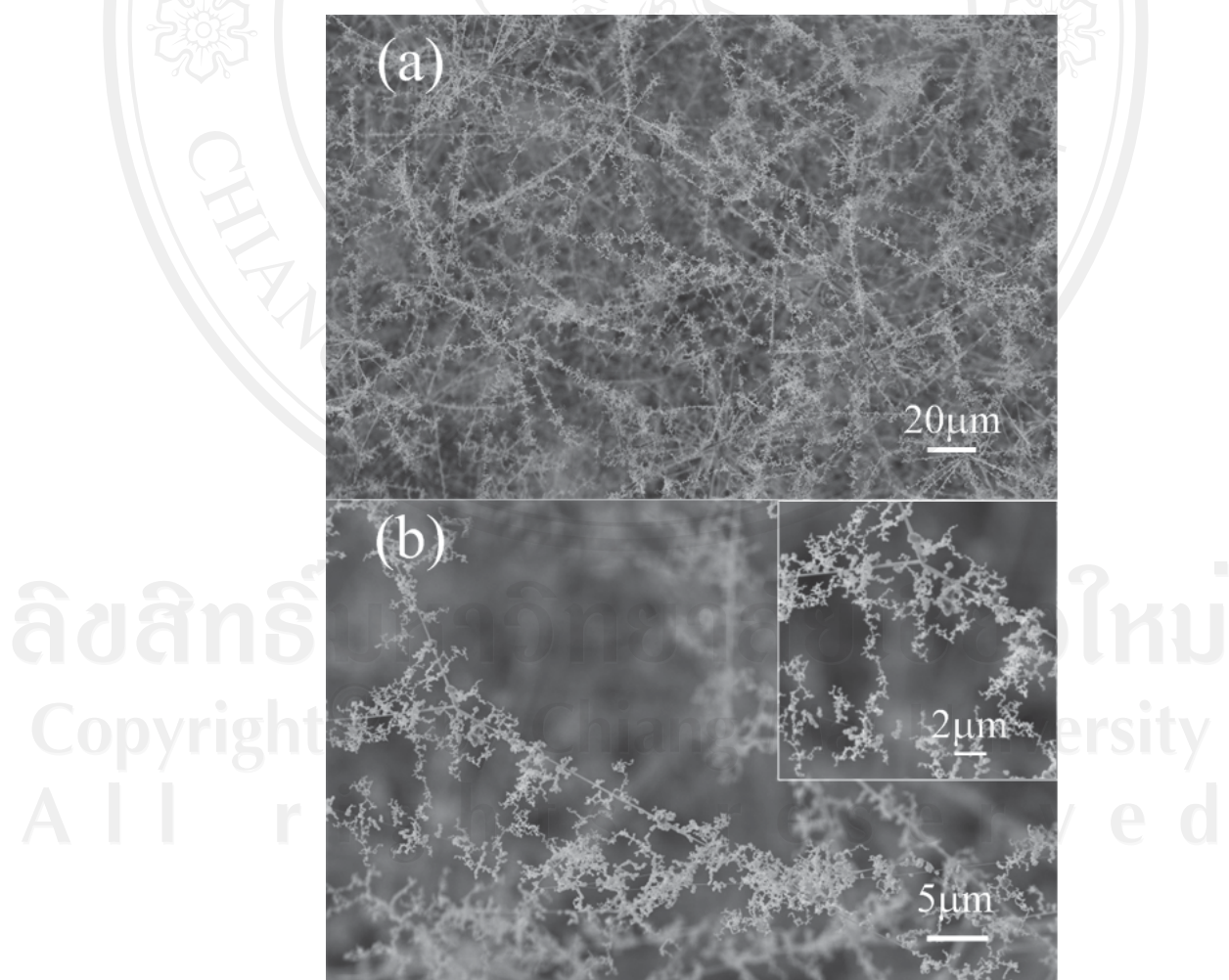


Figure 1

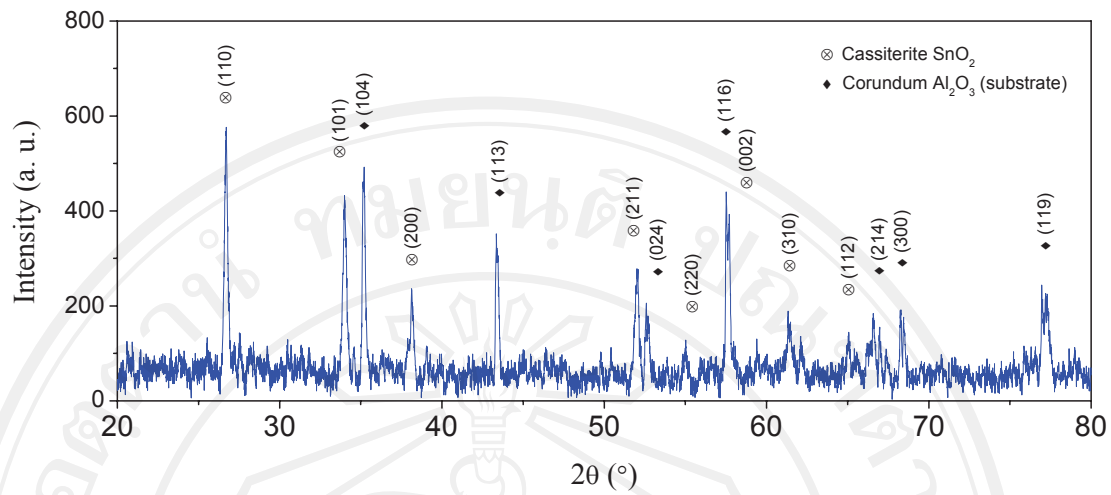


Figure 2

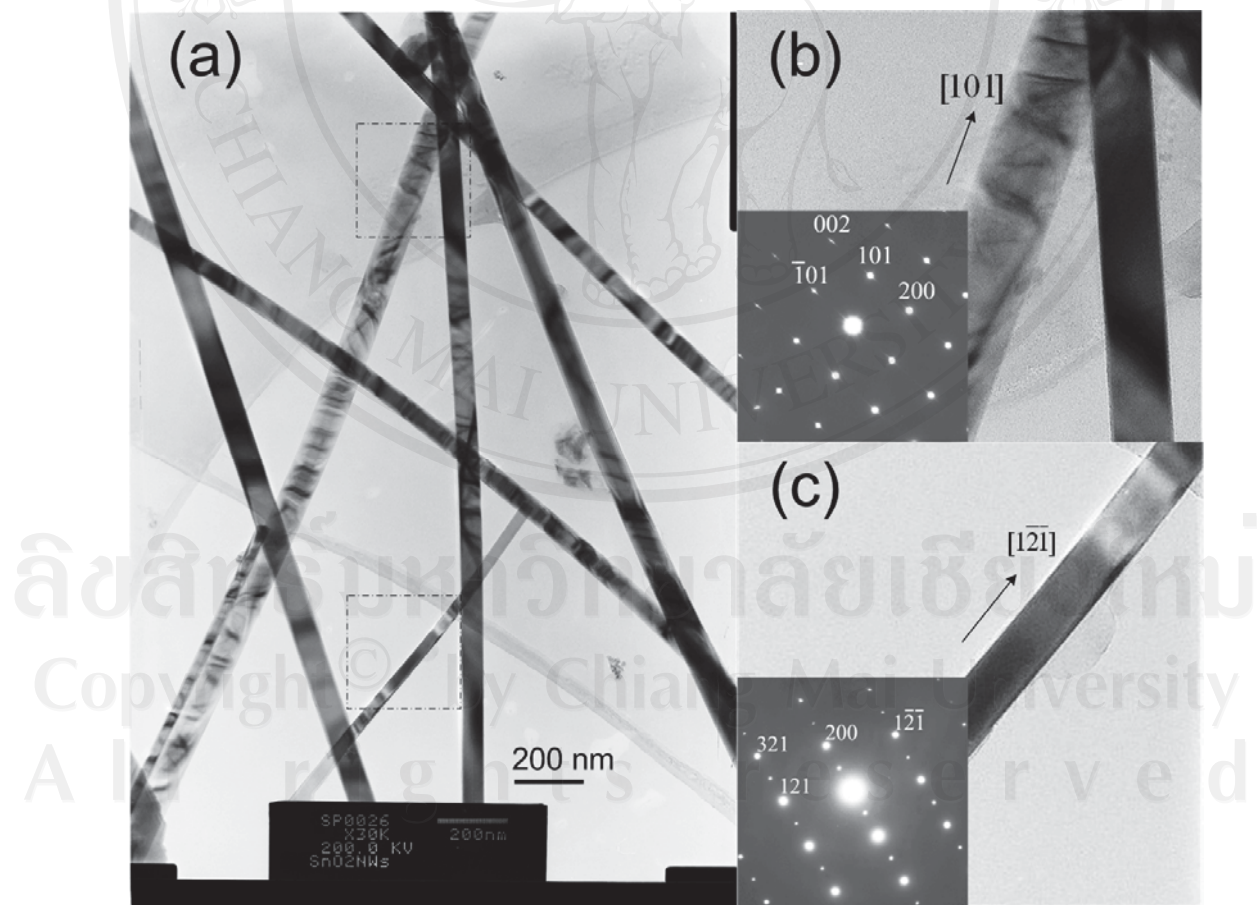


Figure 3

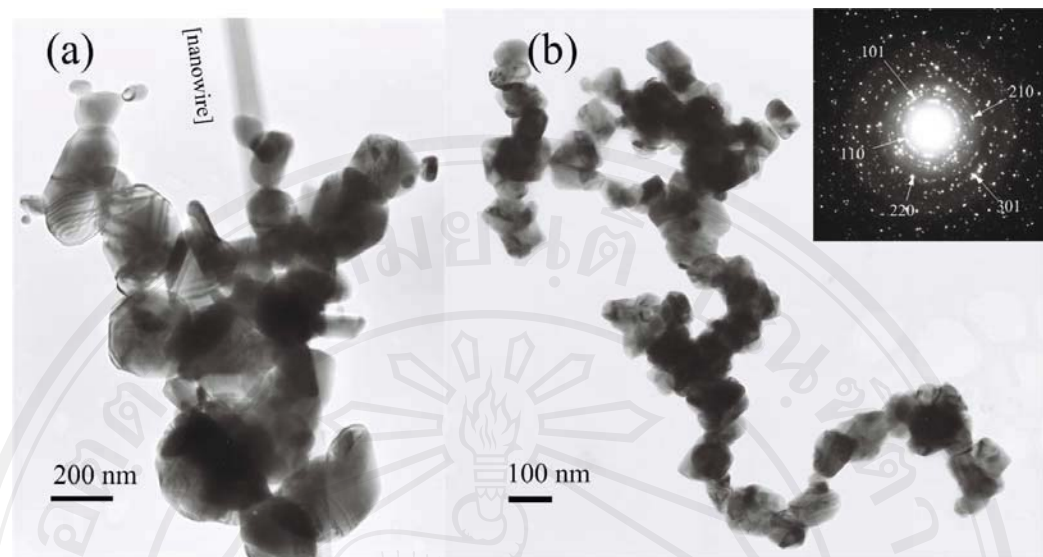


Figure 4

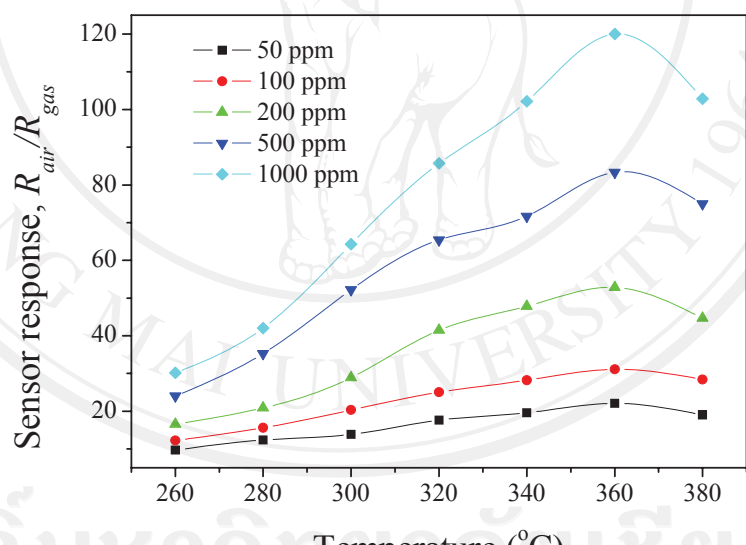


Figure 5

Copyright[©] by Chiang Mai University
All rights reserved

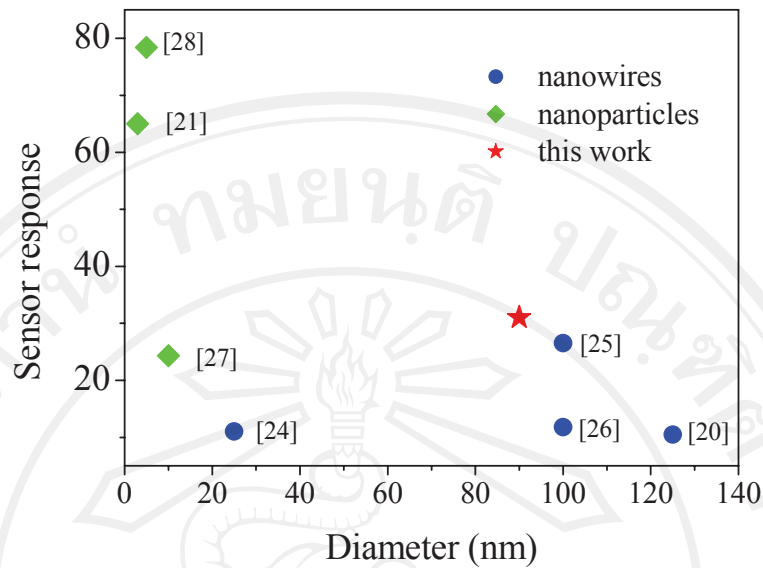


Figure 6

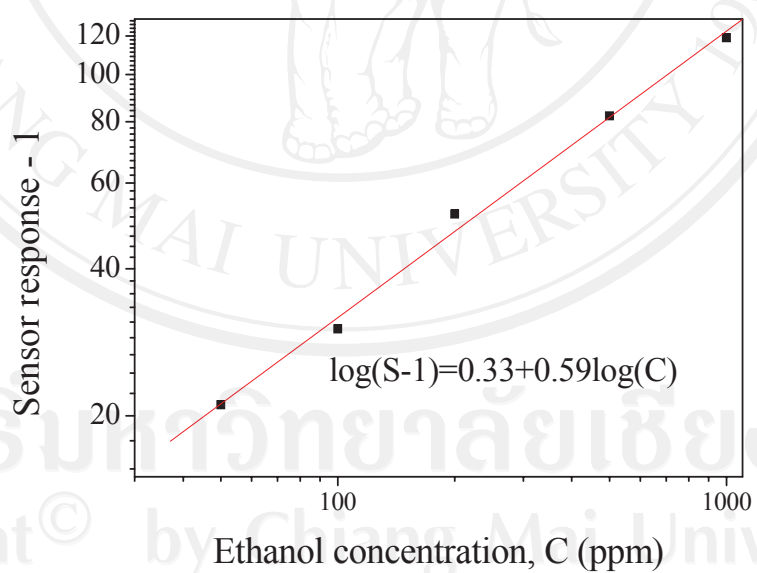


Figure 7

CURRICURUM VITAE

Name/Surname: Mr. Surachet Phadungdhitdhada

Date of birth: 24 November 1978

Corresponding e-mail address: surelity@gmail.com and surelity@hotmail.com

Educational background:

1998–2001 B.Sc (Physics), Department of Physics, Faculty of Science, Chiang Mai University.

Project title: *The Study of the Hot-cathode Arc-discharge Ion Source of Gas Type of Varian Ion Implanter.*

Advisor: Assoc. Prof. Dr. Somsorn Singkarat

2002–2010 Ph.D. (Physics), Department of Physics and Materials Science, Faculty of Science, Chiang Mai University.

Thesis title: *Fabrication of Array-based Tin/Molybdenum Oxide Sensor for E-nose Application.*

Advisor: Assoc. Prof. Dr. Nikorn Mangkorntong

Asst. Prof. Dr. Duangmanee Wongratanaphisan

Scholarships:

1. Financial support via the Grants for Development for New Faculty Staff (GDNFS) Scholarship from the Commission on Higher Education, Ministry of Education, Thailand, 2002-2008.
2. Financial support via the NANOTEC, NSTDA, Ministry of Science and Technology, Thailand, through Network for Excellence in Functional Nanomaterials, Chiang Mai University, Thailand.

Experience:

Research training for study of e-nose applications in School of Chemistry, University of New South Wales, Sydney, Australia, January 2008 – January 2009.

Publications:

1. S. Phadungdhitidhada, P. Mangkorntong, S. Choopun, and N. Mangkorntong, “Raman scattering and electrical conductivity of nitrogen implanted MoO_3 whisker”, *Ceram. Int.* 34 (2008) 1121-1125.
2. S. Phadungdhitidhada, P. Mangkorntong, S. Choopun, N. Mangkorntong, and D. Wongratanaaphisan, “Synthesis of MoO_3 nanobelts by medium energy nitrogen ion implantation”, *Mater. Lett.* 65 (2011) 568-571.

Conference attendances/Presentations:

1. S. Phadungdhitidhada, P. Mangkorntong, S. Towta, S. Tanunchai, S. Wongsila, S. Choopun, and N. Mangkorntong, *Growth of molybdenum trioxide nanowhiskers by vapor transport method*, Poster Presentation, The 30th Congress on Science and Technology of Thailand, 19-21 October 2004, Bangkok, Thailand.
2. S. Phadungdhitidhada, P. Mangkorntong, S. Choopun, and N. Mangkorntong, *Raman scattering and electrical conductivity of nitrogen implanted MoO₃ whisker*, Poster Presentation, 5th Asian Meeting on Electroceramics, 10-14 December 2006, Bangkok, Thailand.
3. S. Phadungdhitidhada, D. Ebrahimi, and D. B. Hibbert, *An optimized e-nose array for discrimination among gases and chemometrics*, Poster Presentation, the 10th Annual Meeting of the Australasian Association for Chemosensory Science (AACSS), 4-6 December 2008, Brisbane, Australia.
4. S. Phadungdhitidhada, A. Gardchereon, D. Wongratanaphisan, D. B. Hibbert, and N. Mangkorntong, *Real-time monitoring and identification of oil spills using an electronic nose*, Oral presentation, AsiaSense2009, 29-31 July 2009, Bangkok, Thailand.
5. S. Phadungdhitidhada, S. Thanasanvorakun, D. Sweatman, N. Mongkorntong and D. Wongratanaphisan, *Fabrication of ethanol gas sensors based on tin dioxide nanowires*, Poster Presentation, Nano-Thailand 2010, 18-20 November 2010, Bangkok, Thailand.